Simulated longitudinal variations in the lower thermospheric nitric oxide induced by nonmigrating tides

Zhipeng Ren,[1] Weixing Wan,[1] Libo Liu,[1] and Jiangang Xiong[1]

Received 17 September 2010; revised 13 January 2011; accepted 18 January 2011; published 1 April 2011.

[1] On the basis of the GCITEM-IGGCAS model and tides from TIMED/SABER observations, the longitudinal variations in the lower thermosphere nitric oxide (NO), which is induced by nonmigrating tides, are investigated. We simulate the intra-annual variation of the NO density and find that equinoctial lower thermospheric NO density shows an obvious wave number 4 longitudinal structure both in equinox and in June solstice and a wave number 3 longitudinal structure in December solstice. These simulation results are consistent with the longitudinal variation observed by Oberheide and Forbes (2008b). The simulations support that the wave number 4 structure in NO density is mainly driven by the eastward propagating nonmigrating diurnal tide with zonal wave number 3, and the wave number 3 structure is mainly driven by the eastward propagating nonmigrating diurnal tide with zonal wave number 2. Our simulations also show that the NO density residuals and the neutral mass density residuals in the height range between 90 and 120 km agree well with each other, and the neutral mass density mainly affects the longitudinal variations of lower thermospheric NO density through modulation of the chemical production rate, e.g., through affecting the chemical reaction between excited nitrogen and molecular oxygen.

Citation: Ren, Z., W. Wan, L. Liu, and J. Xiong (2011), Simulated longitudinal variations in the lower thermospheric nitric oxide induced by nonmigrating tides, *J. Geophys. Res.*, *116*, A04301, doi:10.1029/2010JA016131.

1. Introduction

[2] Solar thermal tides are global-scale atmospheric oscillations in neutral temperature, wind, and density with periods that are subharmonics of a solar day. They mainly originate in the troposphere and stratosphere, and are primarily forced by heating due to absorption of solar radiation at various levels by atmospheric water vapor and ozone. Tides can propagate upward to higher altitudes, and grow exponentially with height. With the effect of damping due to eddy and molecular dissipation, the upward propagating tides achieve their maximum amplitudes in the mesopause–lower thermosphere region (MLT, about 80~150 km). Generally, tide amplitudes are the largest of all the atmospheric oscillations (including Gravity, Planetary and Tidal Waves) in MLT region, and often dominate the thermal and dynamical structure of this region [e.g., *Forbes*, 1995]. Due to eddy and molecular dissipation, tides may dissipate within the MLT region, deposit momentum and energy, and mix atmospheric species or nonlinearly interact with the other waves or with the mean flow, generating additional wave activity [e.g., *Forbes et al.*, 1993]. Through impacting the wind fields and the mixing, tides can affect the density of different neutral atmospheric species, such as NO, O, CO_2, O_3 and water vapor, and thus affect the energy budget either by radiating, or by absorbing solar radiation. Through impacting the neutral wind fields at *E* region altitude, tide can also affect the ionospheric dynamo, and modulate the midlatitude and low-latitude ionospheric electric fields [e.g., *Richmond*, 1995]. Recent investigations showed that tides can as well propagate directly up to thermospheric heights [e.g., *Oberheide et al.*, 2009]. Either through complex coupling mechanisms or through direct propagation, these MLT processes can affect the whole ionosphere-thermosphere system.

[3] Recently, researches based on the observations made by the SABER and TIDI instruments onboard the TIMED satellite have provided new insight into tidal phenomena in MLT region, and have revealed the climatology and the spatiotemporal distributions of the most important tidal components in temperature, and zonal and meridional winds, respectively [e.g., *Forbes et al.*, 2006, 2008; *Oberheide et al.*, 2006, 2007; *Oberheide and Forbes*, 2008a; *Zhang et al.*, 2006]. Expressly, these scientists studied the climatology of the nonmigrating (nonsunsynchronous) tides [e.g., *Forbes et al.*, 2006, 2008; *Oberheide et al.*, 2006, 2007; *Zhang et al.*, 2006], and suggested that nonmigrating tide components are much larger than previous anticipated and often exceed the migrating (sunsynchronous) tide counterparts. The nonmigrating tides give rise to longitudinal variations in local time structures of horizontal winds and temperatures, and greatly affect the longitudinal variations in the MLT region. Through coupling mechanisms (such as the ionospheric dynamo), nonmigrating tides play important

[1]Beijing National Observatory of Space Environment, Institute of Geology and Geophysics, Chinese Academy of Sciences, Beijing, China.

0148-0227/11/2010JA016131

roles in the origination of the longitudinal variations in the upper atmosphere. Thus, many researchers recently paid considerable attention to these nonmigrating tides. For example, because there are growing observational evidences that it is the main source of the prominent wave number 4 structure in the night *F* region electron density observed by *Sagawa et al.* [2005] and in the thermospheric winds observed by *Häusler and Lühr* [2009], the eastward propagating nonmigrating diurnal tide with zonal wave number 3 (DE3) has recently attracted a considerable attention.

[4] DE3, which is excited in the troposphere by latent heat release in deep convective tropical clouds, can achieves large amplitude in the MLT region, and sometimes is the largest component of the diurnal tide in that region. *Immel et al.* [2006] first proposed a production mechanism of the ionospheric wave number 4 longitudinal structure, and suggested that DE3 is the main source of this structure. They suggested that the DE3 tide, when propagates into the ionospheric *E* region, can affect the dynamos and lead to modulations on the ionospheric zonal electric fields and vertical plasma drifts. Then the modulated plasma drifts further induce the motion and redistribution of the ionospheric plasma in *F* region and finally produce the observed ionospheric wave number 4 longitudinal structure. This idea has been supported by recent model simulations [e.g., *Hagan et al.*, 2007, 2009; *England et al.*, 2008, 2010; *Jin et al.*, 2008; *Ren et al.*, 2010] and data analysis [e.g., *Lin et al.*, 2007a, 2007b; *Liu and Watanabe*, 2008; *Kil et al.*, 2008; *Pedatella et al.*, 2008; *Ren et al.*, 2008a, 2009a; *Scherliess et al.*, 2008; *Wan et al.*, 2008; *Liu et al.*, 2009]. Except of the ionospheric plasma density parameters, the obvious wave number 4 longitudinal structures have also been found in the other ionospheric and thermospheric parameters, such as the equatorial electrojet (EEJ), the vertical $\mathbf{E} \times \mathbf{B}$ plasma drifts, the plasma bubble occurrence rates, the electron temperature, the vertical scale height, the lower thermospheric nitric oxide (NO) density, *F* region zonal neutral wind and thermospheric O/N2 ratio [e.g., *England et al.*, 2006; *Häusler et al.*, 2007; *Fejer et al.*, 2008; *Hartman and Heelis*, 2007; *Kil et al.*, 2007; *Lühr et al.*, 2007, 2008; *Li et al.*, 2008; *Liu et al.*, 2008; *Oberheide and Forbes*, 2008b; *Ren et al.*, 2008a, 2009a; *He et al.*, 2010; *Zhang et al.*, 2010]. These researches suggested that DE3 can affect the whole coupled ionosphere-thermosphere system. However, except DE3, researchers also noticed the signals of the other nonmigrating tides (e.g., DE2 and SE1) in the ionosphere-thermosphere system [e.g., *Oberheide and Forbes*, 2008b; *Pedatella et al.*, 2008; *Kil et al.*, 2010]. For example, *Oberheide and Forbes* [2008b] pointed out that the combination of DE3, DE2 (eastward propagating nonmigrating diurnal tide with zonal wave number 2) and SE1 (eastward propagating nonmigrating semidiurnal tide with zonal wave number 1) cause the observed longitudinal variation of NO density in the lower thermosphere.

[5] NO is an important species in the thermosphere. In recent years, increasing attention has been paid to the abundance and variability of NO in the atmosphere for several reasons. First, radiative emission at 5.3 μm from NO is an important cooling mechanism above 120 km altitude [*Kockarts*, 1980], can reduce the heating efficiency near 130 km by a factor of 4 in the summer hemisphere [*Richards et al.*, 1982]. The increase of NO by auroral sources also limits the thermospheric temperature increase during geomagnetic storms [*Maeda et al.*, 1989]. Second, as its low ionization threshold (ionization potential 9.26 eV), ionization of NO by solar Lyman alpha has a direct impact on the ion composition in the *E* region and *D* region. Finally, the descent of thermospheric NO is thought to be one coupling mechanism between the upper and lower atmosphere [e.g., *Siskind*, 2000]. Thermospheric NO exhibits significant variations with altitude, latitude, longitude, local time, season, solar cycle, and auroral activity. Owing to its chemical and radiative processes, NO variability can have a significant impact on the structure and energetics of the ionosphere-thermosphere system. Recently, global observations of the thermospheric NO have been made from the Student Nitric Oxide Explorer (SNOE), a low-altitude, polar-orbiting satellite [*Barth et al.*, 2003, 2009; *Barth and Bailey*, 2004]. Based on the observations of SNOE, *Oberheide and Forbes* [2008b] found that the nonmigrating tides have a significant impact on NO variability in the lower thermosphere. They found wave number 4 like longitude variations in NO density between March and October and wave number 3 like longitude variations in December and January in the range between 30°S–30°N and 100–135 km. They suggested that the DE3 tide cause the observed wave number 4 variation, and the combination of the DE2 tide and the SE1 tide causes the observed wave number 3 variation. In this paper, we will simulate the influence of the nonmigrating tides on the longitudinal variations of NO in the lower thermosphere with the GCITEM-IGGCAS model.

2. Model Descriptions and Inputs

[6] To simulate the complex and highly coupled physical and chemical processes in the ionosphere-thermosphere system, a new global coupled ionosphere-thermosphere model (Global Coupled Ionosphere-Thermosphere-Electrodynamics Model, Institute of Geology and Geophysics, Chinese Academy of Sciences, GCITEM-IGGCAS) was developed at the Institute of Geology and Geophysics, Chinese Academy of Sciences [*Ren et al.*, 2009b]. GCITEM-IGGCAS is a three-dimensional (3-D) code with 5° latitude by 7.5° longitude cells in a spherical geographical coordinate system, which bases on an altitude grid. This model self-consistently calculates the time-dependent 3-D structures of the main thermospheric and ionospheric parameters in the height range from 90 to 600 km, including neutral number density of major species O_2, N_2, and O and minor species N (^{2}D), N(^{4}S), NO, He and Ar; ion number densities of O^+, O_2^+, N_2^+, NO^+, N^+ and electrons; neutral, electron and ion temperature; and neutral wind vectors. It also self-consistently calculates the midlatitude and low-latitude ionospheric electric field using the TIDM-IGGCAS-II model [*Ren et al.*, 2008b]. GCITEM-IGGCAS can reproduce the main features of the thermosphere and ionosphere. The details of GCITEM-IGGCAS model are given by *Ren et al.* [2009b].

[7] We will use the GCITEM-IGGCAS model in this work. The following simulations are all performed for medium solar flux level, corresponding to a solar 10.7 cm flux index ($F_{10.7}$) of 140 and an 81 day average value of $F_{10.7}$ of 140, and geomagnetic quiet inputs with a cross cap potential of 20 kV and auroral particle precipitation with a hemispheric power of 10 GW. An IGRF geomagnetic field

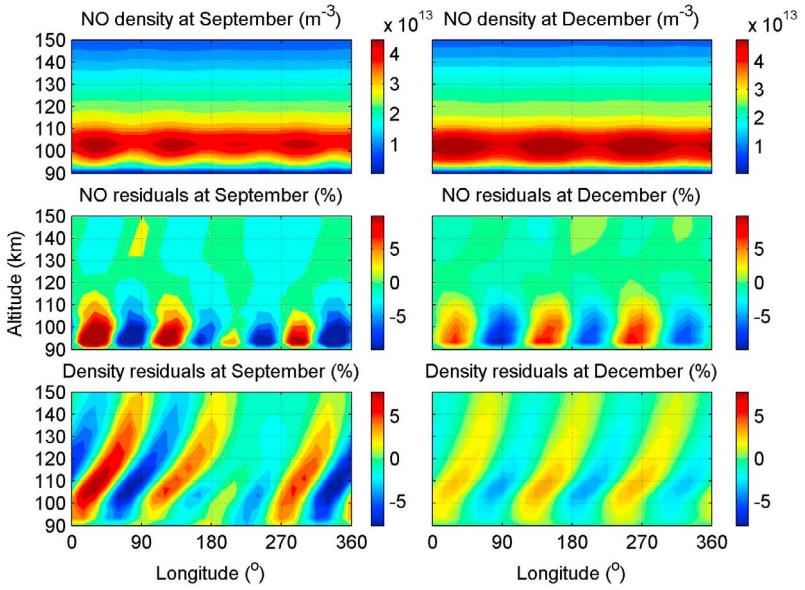

Figure 1. Longitudinal and altitudinal variations of (top) the simulated NO densities, (middle) the NO density residuals, and (bottom) the neutral mass density residuals at equator for (left) September and (right) December.

is used in these simulations. The initial conditions of these simulations are all from empirical models. The initial conditions of the neutral temperature and neutral number density of O_2, N_2, O, $N(^4S)$, He and Ar are from the MSIS00 empirical model [*Hedin*, 1991], and the *Titheridge* [1997] empirical model provides the initial condition of the NO number density. The initial conditions of the electron temperature, ion temperature, ion number densities of O^+, O_2^+, NO^+ and electron density are from the IRI2000 empirical model [*Bilitza*, 2001]. The neutral temperature and compositions from MSIS00 empirical model are used at the low boundary (90 km altitude). However, we remove the diurnal and semidiurnal tide of the MSIS00 empirical model, and add the neutral temperature tides, and neutral density tides from TIMED/SABER observations at the low boundary.

[8] The TIMED/SABER instrument is a 10-channel radiometer that retrieves the kinetic temperature from 20 km to 120 km altitude based on the CO_2 15.4 μm limb emission measurements [*Russell et al.*, 1999], and has continuously taken data since March 2002. The TIMED/SABER observations using in this paper are produced by the National Center for Atmospheric Research (NCAR, see http://saber.gats-inc.com). Here, we mainly use the observations from March 2002 to early November 2007. The TIMED satellite is a slowly processing satellite, and the 24 h local times coverage of the TIMED/SABER observations is obtained every 60 days. Thus, the temperature and number density at 90 km from TIMED/SABER are first binned every 5° in latitude into 5° wide geographical latitude bins from a 60 day running window centered on each day. Then, tides in the TIMED/SABER data are derived by means of a two-dimensional Fourier transform of the data set for different latitude bins. Finally, we bin them into 12 one-month wide bins, and the temperature and number density tide for different months are obtained. As *Oberheide and Forbes* [2008b] suggested that the combination of DE3, DE2 and SE1 causes the observed longitudinal variation in NO density in the lower thermosphere, we add the migrating diurnal and semidiurnal tides, and the nonmigrating DE3, DE2 and SE1 tides from TIMED/SABER observations to the low boundary.

3. Result and Discussions

[9] We simulated the thermospheric NO densities in different conditions. *Oberheide and Forbes* [2008b] showed the thermospheric NO densities at September and December based on the SNOE observations. To make it comparable with *Oberheide and Forbes*' [2008b] observations, Figure 1 (top) also shows the longitudinal/altitudinal structures of the simulated NO densities for September (left) and December (right). To compare with the observations of *Oberheide and Forbes* [2008b], all these plots show the results at 1030 LT. Similar to the observations of *Oberheide and Forbes* [2008b], an obvious wave number 4 longitudinal structure is shown at September NO density, and the December NO density shows a wave number 3 structure instead the wave number 4 structure. Through subtraction of and division by the zonal mean, we get the percentage residuals for these 2 months and show them in Figure 1 (middle). As shown in these plots, the peak-to-peak variations of these longitudinal structures can approach 30%, and the longitudinal variations in September are stronger than that in December. The wave number 4/wave number 3 structures in September and in December are stronger between 90 and 110 km than above 110 km, and the longitudinal variations at altitudes above 110 km are weaker and show some phase differences from the phase between 90 and 110 km. The maximum between 180° and 270° in the September NO residuals are much less pronounced than at the other longitudes. Similar to *Oberheide and Forbes* [2008b], through subtraction of and division by the zonal mean, we also show the corresponding simulated neutral mass density residuals at 1030 LT at

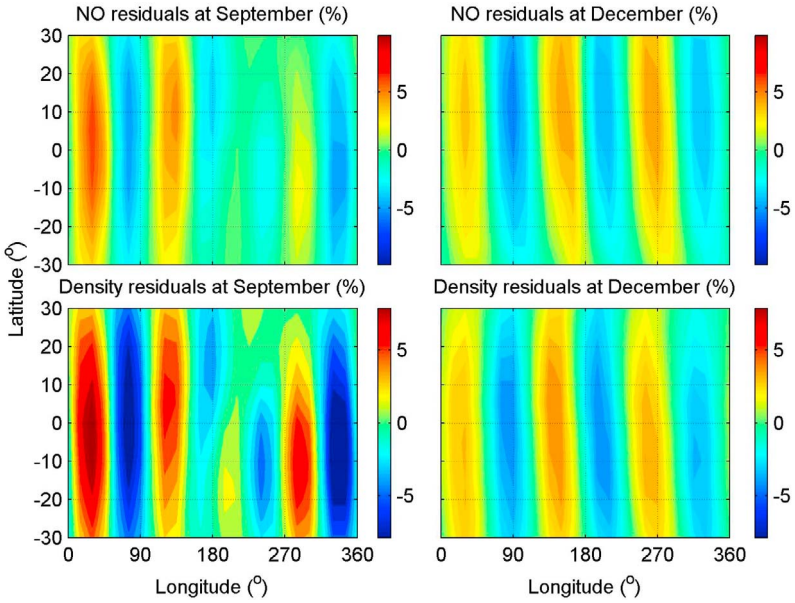

Figure 2. Latitudinal and longitudinal variations of (top) the NO density residuals and (bottom) the neutral mass density residuals at 107 km for (left) September and (right) December.

Figure 1 (bottom). The neutral mass density residuals also show wave number 4/wave number 3 patterns in September and in December, and the longitudinal variations in September are stronger than that in December. The peak-to-peak variations of these longitudinal structures can approach 15%. Expressly, the phases of the NO density residuals and the neutral mass density residuals in the height range between 90 and 120 km agree well with each other. However, different from the longitudinal structures in NO density, the wave number 4/wave number 3 structures in neutral mass density residuals show a maximum peak-to-peak variation between 90 and 140 km, e.g., reaching to higher altitudes than the variation pattern in the neutral density.

[10] As suggested by *Oberheide and Forbes* [2008b], the striking match between the longitudinal variations in NO density and in neutral mass density suggests that the longitudinal variations in the 90–120 km NO data are caused by tide in the neutral mass density. To examine this idea, we also show the latitude/longitude cuts between −30° latitude and 30° latitude at 1030 LT and at 107 km for September and December in Figure 2. Figure 2 (top) shows the NO density residuals, and Figure 2 (bottom) shows the neutral mass density residuals. As shown in Figure 2, although there are some differences, the wave number 4/wave number 3 pattern in NO density in September (left)/December (right) persists roughly at all latitudes and is well reproduced by the neutral mass density residuals. Expressly, we notice that there is a hemispheric asymmetry of the NO density residuals in the longitudinal range between 150°E and 270°E in September, and similar structure can also be found in the neutral mass density residuals. However, although the wave number 3 pattern in NO density in December at northern (winter) hemisphere is stronger than that at southern (summer) hemisphere, this phenomenon is not shown in the neutral mass density residuals. The results of these simulations suggested that the longitudinal variations in the NO density may be caused by the longitudinal variations in neutral mass density.

[11] To further examine the relation between the NO density and the neutral mass density, we also simulate the intra-annual variations of the NO density and of the neutral mass density. Figure 3 shows the intra-annual and longitudinal variations of the NO density residuals and of the neutral mass density residuals at 1030 LT, at the equator and at 107 km. As shown in Figure 3, the NO density residuals and the neutral mass density residuals show similar intra-annual and longitudinal variations. They both show a wave number 4 pattern between March and October, and a wave number 3 pattern at January and at December. At February and November, they both transit between wave number 3 pattern and the wave number 4 pattern. Figure 3 also shows that the phase of the wave number 4 pattern of the NO density residuals obviously changes with the month, and similar phase variation can also be seen in the wave number 4 pattern of the neutral mass density residuals. The similar intra-annual variations also support the suggestion that the longitudinal variations in the NO density may be caused by the longitudinal variations in neutral mass density.

[12] *Oberheide and Forbes* [2008b] suggested that the observed wave number 4 variations in NO density are caused by the DE3 tide and the observed wave number 3 variation in NO density are caused by the DE2 and SE1 tide. The s in DEs and SEs both describe the zonal wave number in UT frame. However, in LT frame, an eastward propagating diurnal/semidiurnal tide of zonal wave number s will be observed as a zonal wave number (s+1)/(s+2). Thus, the DE3 tide can drive the wave number 4 structure in neutral mass density, and the DE2 and SE1 tide both can drive the wave number 3 structure in neutral mass density. However, as different kinds of tide can nonlinearly interact with each other and with the mean flow, we also need examine the influence of each of these tides on the NO density. Through

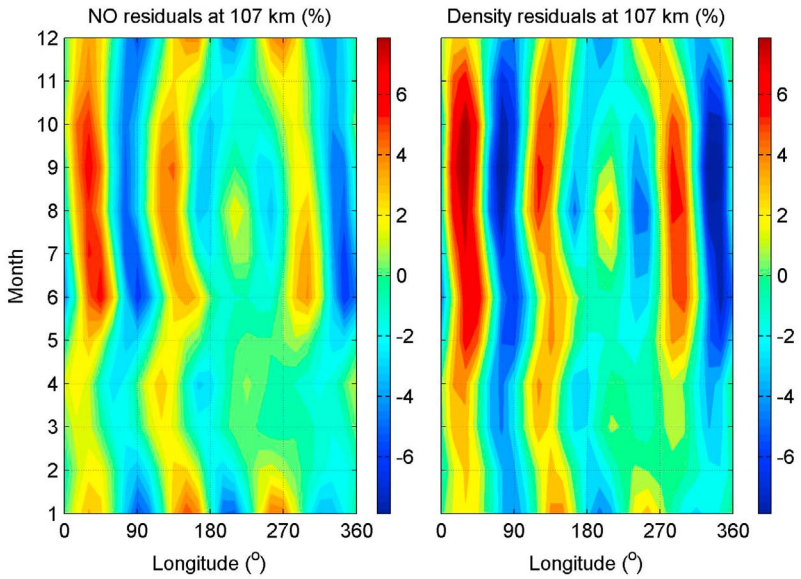

Figure 3. Intra-annual and longitudinal variations of (left) the NO density residuals and (right) the neutral mass density residuals at 107 km and at equator.

adding different nonmigrating tide at the low boundary, we examine the influence of each of the tides. We first simulate the NO density at September in two conditions: (1) without nonmigrating tide at the low boundary and (2) only with DE3 nonmigrating tide at the low boundary. Similar to Figure 1, Figure 4 shows the longitudinal/altitudinal structures of the simulated NO density (top), the NO density residuals (middle), and the neutral mass density residuals (bottom) in these two simulations. As shown in Figure 4, NO density in case 2 shows an obvious wave number 4 structure and that in case 1 does not show similar structure. Through comparing Figures 1 and 4, we find that the wave number 4 structures driven by DE3 and driven by all tides together are very similar with each other, and this suggests

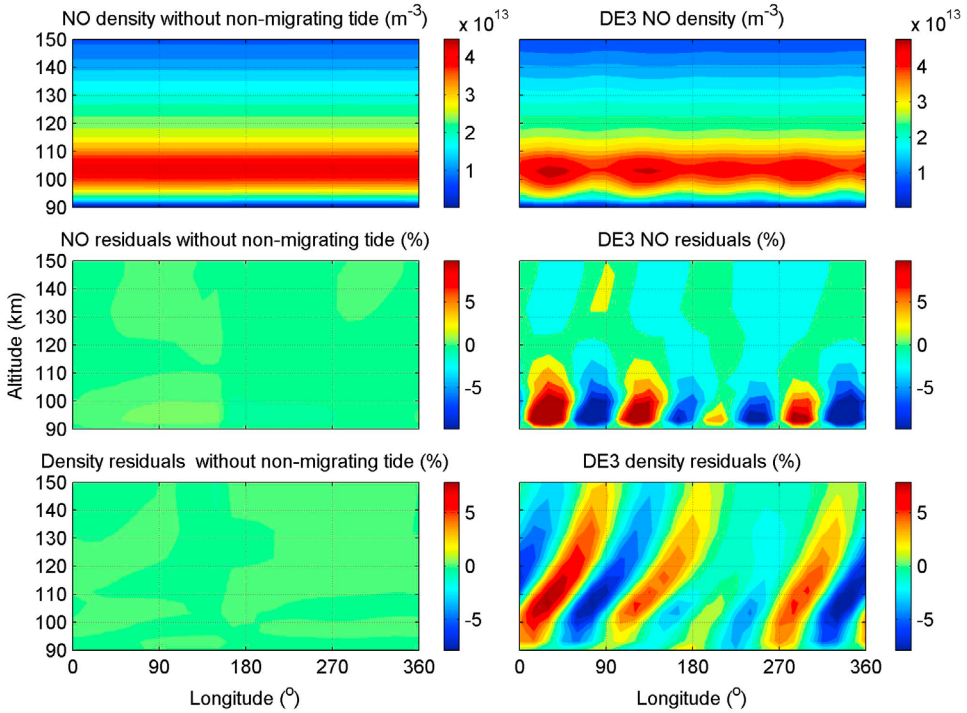

Figure 4. Longitudinal and altitudinal variations of (top) the simulated NO densities, (middle) the NO density residuals, and (bottom) the neutral mass density residuals at equator for September. (left) Results without nonmigrating tide and (right) results with only DE3 tide.

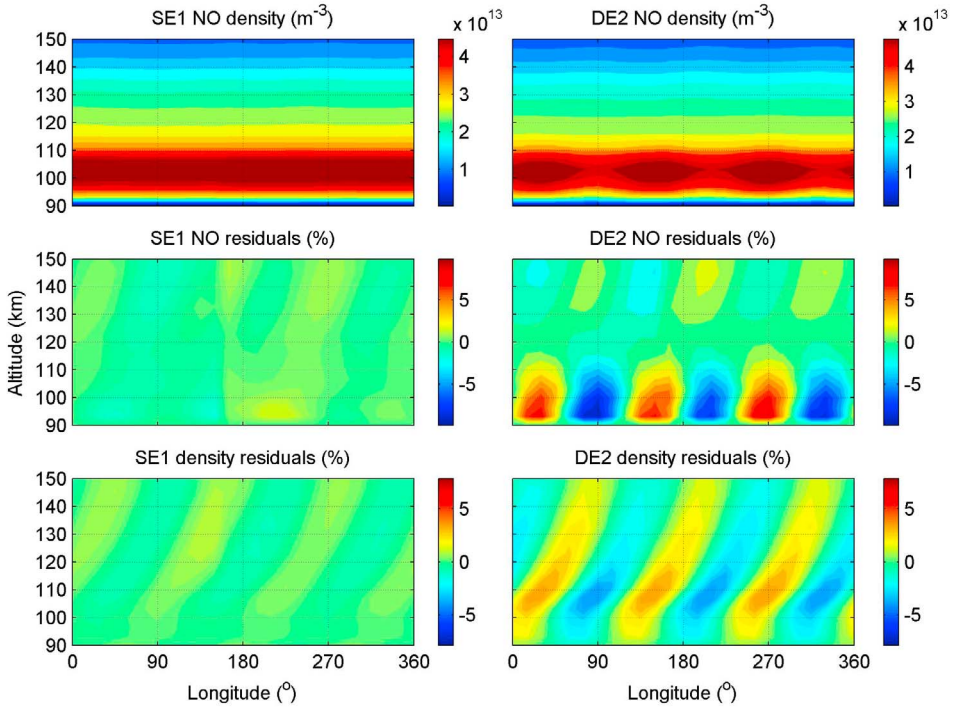

Figure 5. Longitudinal and altitudinal variations of (top) the simulated NO densities, (middle) the NO density residuals, and (bottom) the neutral mass density residuals at equator for September. (left) Results with only SE1 tide and (right) results with only DE2 tide.

that the wave number 4 structures in NO density and in neutral mass density are both driven by the DE3 tide. We also simulate the NO density at December in two conditions: (1) only with SE1 tide at the low boundary and (2) only with DE2 tide at the low boundary. Similar to Figures 4 and 1, Figure 5 shows the longitudinal/altitudinal structures of the simulated NO density (top), the NO density residuals (middle), and the neutral mass density residuals (bottom). As shown in Figure 5, NO density in case 2 shows an obvious wave number 3 structure and the wave number 3 structure in case 1 is very weak. Through comparing Figures 1 and 5, we will find that the wave number 3 structures driven by DE2 and driven by all tides together are very similar with each other, and this suggests that the wave number 3 structures in NO density and in neutral mass density are both mainly driven by the DE2 tide.

[13] Although the longitudinal variations in the NO density may be caused by the longitudinal variations in neutral mass density, we still do not know their physical mechanism. Molecular and eddy transports, vertical and horizontal transport by thermospheric wind and the chemical processes all can affect the NO density in the lower thermosphere. *Barth* [1995] and *Barth and Bailey* [2004] both suggested that the photochemical processes greatly affect the NO density in the lower thermosphere. The chemical process of NO is complex, and Table 1 shows the main NO chemical reactions in the GCITEM-IGGCAS model. *Barth* [1995] had pointed out that the principal source of NO in the lower thermosphere is the chemical reaction between excited atomic nitrogen ($N(^2D)$) and molecular oxygen (O_2) (R1), and the reaction of ground state atomic nitrogen ($N(^4S)$) with O_2 (R4) is significant only in the higher thermosphere above 130 km. *Barth* [1995] also suggested that the reaction between NO and $N(^4S)$ (R2) is the principal loss mechanism for NO in the lower thermosphere, and the reaction of NO with ionized molecular oxygen (O_2^+) (R3) also play an important role in the loss of NO in the lower thermosphere below 120 km. To examine the influence the different chemical reactions (R1, R2 and R3), we simulate the NO density at September in three conditions: (1) without reaction R1, (2) without reaction R2, and (3) without reaction R3. Figure 6 shows the longitudinal/altitudinal structures of the simulated NO density at the equator in different simulations. For comparison, we also show the simulation results with all reactions in Figure 6. As shown in Figure 6, when we remove the reaction R2 or R3, although the NO density are obviously larger than that in basic condition, the relative longitudinal variations only show little enhancement. However, when we remove the reaction R1, the wave number 4 structures between 90 and 120 km nearly disappear. This result sug-

Table 1. NO Chemical Reactions in GCITEM-IGGCAS

NO Chemical Reactions	Reaction Number
$N(^4S) + O_2 \rightarrow NO + O$	R4
$N(^2D) + O_2 \rightarrow NO + O(^1D)$	R1
$NO + h\nu\ (Ly - \alpha) \rightarrow NO^+ + e$	
$NO + h\nu\ (SRB) \rightarrow N(^4S) + O$	
$N(^4S) + NO \rightarrow N_2 + O$	R2
$N(^2D) + NO \rightarrow N_2 + O$	
$O_2^+ + NO \rightarrow NO^+ + O_2$	R3
$O^+(^2P) + N_2 \rightarrow N^+ + NO$	

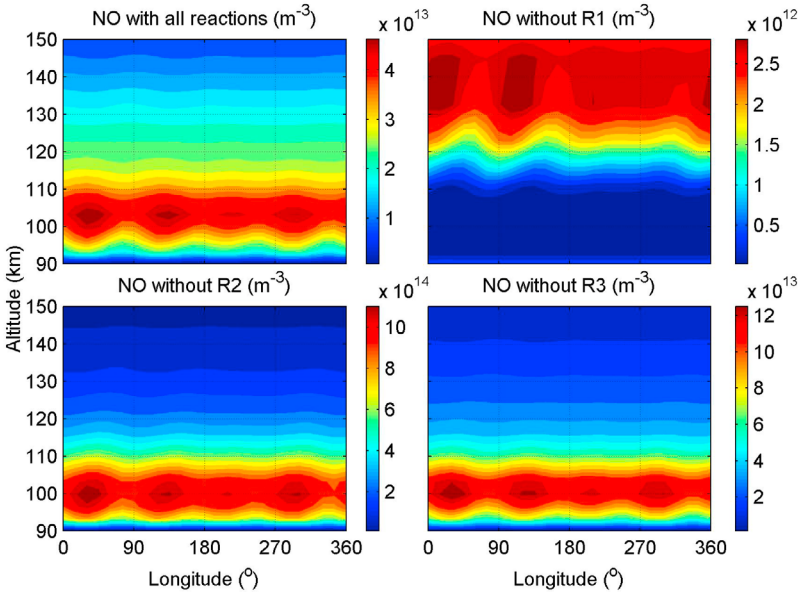

Figure 6. Longitudinal and altitudinal variations of the simulated NO densities at equator for September. The four plots show the results with all chemical reactions, without reaction R1, without reaction R2, and without reaction R3.

gests that the NO in the lower thermosphere is mainly controlled by the reaction R1 which is the chemical reaction between excited atomic nitrogen and molecular oxygen. This means that the longitudinal variations of the neutral mass density (molecular nitrogen density) may affect the $N(^2D)$ density in the lower thermosphere, and modulate the longitudinal variations of lower thermospheric NO density. Although the transport processes and chemical loss certainly also affects the NO density, the longitudinal variations in the lower thermospheric NO density are mainly controlled by the chemical production processes, e.g., the source of NO as the chemical reaction between excited nitrogen and molecular oxygen.

4. Summary and Conclusion

[14] In the presented work, using GCITEM-IGGCAS model and tides from TIMED/SABER observations, we investigate the longitudinal variations of the lower thermospheric nitric oxide (NO), which is induced by nonmigrating tides. We simulated the intra-annual variation of the NO density, and find that equinoctial lower thermospheric NO density shows an obvious wave number 4 longitudinal structure both in equinox and in June solstice, and a wave number 3 longitudinal structure in December solstice. These simulation results are consistent with the intra-annual variations observed by *Oberheide and Forbes* [2008b]. Our simulations support that the wave number 4 structure in NO density is mainly driven by the DE3 tide, and the wave number 3 structure is mainly driven by the DE2 tide. Our simulations also show that the NO density residuals and the neutral mass density residuals in the height range between 90 and 120 km agree well with each other, and the neutral mass density affect the longitudinal variations of lower thermospheric NO density through modulation the chemical production rate, e.g., through affecting the chemical reaction between excited nitrogen and molecular oxygen.

[15] **Acknowledgments.** We are grateful to the SABER team for the access to the data on http://saber.gats-inc.com. This work is supported by National Science Foundation of China (41004070, 40974090, 40725014), National Important Basic Research Project (2011CB811405), Knowledge Innovation Program of the Chinese Academy of Sciences, and China Postdoctoral Science Foundation.

[16] Robert Lysak thanks the reviewers for their assistance in evaluating this paper.

References

Barth, C. A. (1995), Nitric oxide in the lower thermosphere, in *The Upper Mesosphere and Lower Thermosphere: A Review of Experiment and Theory*, *Geophys. Monogr. Ser.*, vol. 87, edited by R. M. Johnson and T. L. Killeen, pp. 225–233, AGU, Washington, D. C.

Barth, C. A., and S. M. Bailey (2004), Comparison of a thermospheric photochemical model with Student Nitric Oxide Explorer (SNOE) observations of nitric oxide, *J. Geophys. Res.*, *109*, A03304, doi:10.1029/2003JA010227.

Barth, C. A., K. D. Mankoff, S. M. Bailey, and S. C. Solomon (2003), Global observations of nitric oxide in the thermosphere, *J. Geophys. Res.*, *108*(A1), 1027, doi:10.1029/2002JA009458.

Barth, C. A., G. Lu, and R. G. Roble (2009), Joule heating and nitric oxide in the thermosphere, *J. Geophys. Res.*, *114*, A05301, doi:10.1029/2008JA013765.

Bilitza, D. (2001), International reference ionosphere 2000, *Radio Sci.*, *36*(2), 261–272.

England, S. L., S. Maus, T. J. Immel, and S. B. Mende (2006), Longitudinal variation of the *E* region electric fields caused by atmospheric tides, *Geophys. Res. Lett.*, *33*, L21105, doi:10.1029/2006GL027465.

England, S. L., T. J. Immel, and J. D. Huba (2008), Modeling the longitudinal variation in the post-sunset far-ultraviolet OI airglow using the SAMI2 model, *J. Geophys. Res.*, *113*, A01309, doi:10.1029/2007JA012536.

England, S. L., T. J. Immel, J. D. Huba, M. E. Hagan, A. Maute, and R. DeMajistre (2010), Modeling of multiple effects of atmospheric tides on the ionosphere: An examination of possible coupling mechanisms responsible for the longitudinal structure of the equatorial ionosphere, *J. Geophys. Res.*, *115*, A05308, doi:10.1029/2009JA014894.

Fejer, B. G., J. W. Jensen, and S.-Y. Su (2008), Quiet time equatorial *F* region vertical plasma drift model derived from ROCSAT-1 observations, *J. Geophys. Res.*, *113*, A05304, doi:10.1029/2007JA012801.

Forbes, J. M. (1995), Tidal and planetary waves, in *The Upper Mesosphere and Lower Thermosphere: A Review of Experiment and Theory*, *Geophys. Monogr. Ser.*, vol. 87, edited by R. M. Johnson and T. L. Killeen, pp. 67–87, AGU, Washington, D. C.

Forbes, J. M., R. G. Roble, and C. Fesen (1993), Acceleration, heating, and compositional mixing of the thermosphere due to upward propagating tides, *J. Geophys. Res.*, *98*(A1), 311–321, doi:10.1029/92JA00442.

Forbes, J. M., J. Russell, S. Miyahara, X. Zhang, S. Palo, M. Mlynczak, C. J. Mertens, and M. E. Hagan (2006), Troposphere-thermosphere tidal coupling as measured by the SABER instrument on TIMED during July–September 2002, *J. Geophys. Res.*, *111*, A10S06, doi:10.1029/2005JA011492.

Forbes, J. M., X. Zhang, S. Palo, J. Russell, C. J. Mertens, and M. Mlynczak (2008), Tidal variability in the ionospheric dynamo region, *J. Geophys. Res.*, *113*, A02310, doi:10.1029/2007JA012737.

Hagan, M. E., A. Maute, R. G. Roble, A. D. Richmond, T. J. Immel, and S. L. England (2007), Connections between deep tropical clouds and the Earth's ionosphere, *Geophys. Res. Lett.*, *34*, L20109, doi:10.1029/2007GL030142.

Hagan, M. E., A. Maute, and R. G. Roble (2009), Tropospheric tidal effects on the middle and upper atmosphere, *J. Geophys. Res.*, *114*, A01302, doi:10.1029/2008JA013637.

Hartman, W. A., and R. A. Heelis (2007), Longitudinal variations in the equatorial vertical drift in the topside ionosphere, *J. Geophys. Res.*, *112*, A03305, doi:10.1029/2006JA011773.

Häusler, K., and H. Lühr (2009), Nonmigrating tidal signals in the upper thermospheric zonal wind at equatorial latitudes as observed by CHAMP, *Ann. Geophys.*, *27*, 2643–2652, doi:10.5194/angeo-27-2643-2009.

Häusler, K., H. Lühr, S. Rentz, and W. Köhler (2007), A statistical analysis of longitudinal dependences of upper thermospheric zonal winds at dip equator latitudes derived from CHAMP, *J. Atmos. Sol. Terr. Phys.*, *69*(12), 1419–1430, doi:10.1016/j.jastp.2007.04.004.

He, M., L. Liu, W. Wan, J. Lei, and B. Zhao (2010), Longitudinal modulation of the O/N_2 column density retrieved from TIMED/GUVI measurement, *Geophys. Res. Lett.*, *37*, L20108, doi:10.1029/2010GL045105.

Hedin, A. E. (1991), Extension of the MSIS thermosphere model into the middle and lower atmosphere, *J. Geophys. Res.*, *96*(A2), 1159–1172, doi:10.1029/90JA02125.

Immel, T. J., E. Sagawa, S. L. England, S. B. Henderson, M. E. Hagan, S. B. Mende, H. U. Frey, C. M. Swenson, and L. J. Paxton (2006), Control of equatorial ionospheric morphology by atmospheric tides, *Geophys. Res. Lett.*, *33*, L15108, doi:10.1029/2006GL026161.

Jin, H., Y. Miyoshi, H. Fujiwara, and H. Shinagawa (2008), Electrodynamics of the formation of ionospheric wave number 4 longitudinal structure, *J. Geophys. Res.*, *113*, A09307, doi:10.1029/2008JA013301.

Kil, H., S.-J. Oh, M. C. Kelley, L. J. Paxton, S. L. England, E. Talaat, K.-W. Min, and S.-Y. Su (2007), Longitudinal structure of the vertical **E** × **B** drift and ion density seen from ROCSAT-1, *Geophys. Res. Lett.*, *34*, L14110, doi:10.1029/2007GL030018.

Kil, H., E. R. Talaat, S.-J. Oh, L. J. Paxton, S. L. England, and S.-J. Su (2008), Wave structures of the plasma density and vertical E × B drift in low-latitude *F* region, *J. Geophys. Res.*, *113*, A09312, doi:10.1029/2008JA013106.

Kil, H., L. J. Paxton, W. K. Lee, Z. Ren, S.-J. Oh, and Y.-S. Kwak (2010), Is DE2 the source of the ionospheric wave number 3 longitudinal structure?, *J. Geophys. Res.*, *115*, A11319, doi:10.1029/2010JA015979.

Kockarts, G. (1980), Nitric oxide cooling in the terrestrial thermosphere, *Geophys. Res. Lett.*, *7*, 137–140, doi:10.1029/GL007i002p00137.

Li, G., B. Ning, L. Liu, B. Zhao, X. Yue, S.-Y. Su, and S. Venkatraman (2008), Correlative study of plasma bubbles, evening equatorial ionization anomaly, and equatorial prereversal **E** × **B** drifts at solar maximum, *Radio Sci.*, *43*, RS4005, doi:10.1029/2007RS003760.

Lin, C. H., W. Wang, M. E. Hagan, C. C. Hsiao, T. J. Immel, M. L. Hsu, J. Y. Liu, L. J. Paxton, T. W. Fang, and C. H. Liu (2007a), Plausible effect of atmospheric tides on the equatorial ionosphere observed by the FORMOSAT-3/COSMIC: Three-dimensional electron density structures, *Geophys. Res. Lett.*, *34*, L11112, doi:10.1029/2007GL029265.

Lin, C. H., C. C. Hsiao, J. Y. Liu, and C. H. Liu (2007b), Longitudinal structure of the equatorial ionosphere: Time evolution of the four-peaked EIA structure, *J. Geophys. Res.*, *112*, A12305, doi:10.1029/2007JA012455.

Liu, H., and S. Watanabe (2008), Seasonal variation of the longitudinal structure of the equatorial ionosphere: Does it reflect tidal influences from below?, *J. Geophys. Res.*, *113*, A08315, doi:10.1029/2008JA013027.

Liu, L., M. He, W. Wan, and M.-L. Zhang (2008), Topside ionospheric scale heights retrieved from Constellation Observing System for Meteorology, Ionosphere, and Climate radio occultation measurements, *J. Geophys. Res.*, *113*, A10304, doi:10.1029/2008JA013490.

Liu, L., B. Zhao, W. Wan, B. Ning, M.-L. Zhang, and M. He (2009), Seasonal variations of the ionospheric electron densities retrieved from Constellation Observing System for Meteorology, Ionosphere, and Climate mission radio occultation measurements, *J. Geophys. Res.*, *114*, A02302, doi:10.1029/2008JA013819.

Lühr, H., K. Häusler, and C. Stolle (2007), Longitudinal variation of *F* region electron density and thermospheric zonal wind caused by atmospheric tides, *Geophys. Res. Lett.*, *34*, L16102, doi:10.1029/2007GL030639.

Lühr, H., M. Rother, K. Häusler, P. Alken, and S. Maus (2008), Influence of nonmigrating tides on the longitudinal variation of the equatorial electrojet, *J. Geophys. Res.*, *113*, A08313, doi:10.1029/2008JA013064.

Maeda, S., T. J. Fuller-Rowell, and D. S. Evans (1989), Zonally averaged dynamical and compositional response of the thermosphere to auroral activity during September 18–24, 1984, *J. Geophys. Res.*, *94*(A12), 16,869–16,883, doi:10.1029/JA094iA12p16869.

Oberheide, J., and J. M. Forbes (2008a), Tidal propagation of deep tropical cloud signatures into the thermosphere, *Geophys. Res. Lett.*, *35*, L04816, doi:10.1029/2007GL032397.

Oberheide, J., and J. M. Forbes (2008b), Thermospheric nitric oxide variability induced by nonmigrating tides, *Geophys. Res. Lett.*, *35*, L16814, doi:10.1029/2008GL034825.

Oberheide, J., Q. Wu, T. L. Killeen, M. E. Hagan, and R. G. Roble (2006), Diurnal nonmigrating tides from TIMED Doppler Interferometer wind data: Monthly climatologies and seasonal variations, *J. Geophys. Res.*, *111*, A10S03, doi:10.1029/2005JA011491.

Oberheide, J., Q. Wu, T. L. Killeen, M. E. Hagan, and R. G. Roble (2007), A climatology of nonmigrating semidiurnal tides from TIMED Doppler Interferometer (TIDI) wind data, *J. Atmos. Sol. Terr. Phys.*, *69*(17–18), 2203–2218, doi:10.1016/j.jastp.2007.05.010.

Oberheide, J., J. M. Forbes, K. Häusler, Q. Wu, and S. L. Bruinsma (2009), Tropospheric tides from 80 to 400 km: Propagation, interannual variability, and solar cycle effects, *J. Geophys. Res.*, *114*, D00I05, doi:10.1029/2009JD012388.

Pedatella, N. M., J. M. Forbes, and J. Oberheide (2008), Intra-annual variability of the low-latitude ionosphere due to nonmigrating tides, *Geophys. Res. Lett.*, *35*, L18104, doi:10.1029/2008GL035332.

Ren, Z., W. Wan, L. Liu, B. Zhao, Y. Wei, X. Yue, and R. A. Heelis (2008a), Longitudinal variations of electron temperature and total ion density in the sunset equatorial topside ionosphere, *Geophys. Res. Lett.*, *35*, L05108, doi:10.1029/2007GL032998.

Ren, Z., W. Wan, Y. Wei, L. Liu, and T. Yu (2008b), A theoretical model for mid- and low-latitude ionospheric electric fields in realistic geomagnetic fields, *Chin. Sci. Bull.*, *53*(24), 3883–3890, doi:10.1007/s11434-008-0404-4.

Ren, Z., W. Wan, L. Liu, and J. Xiong (2009a), Intra-annual variation of wavenumber-4 structure of vertical **E** × **B** drifts in the equatorial ionosphere seen from ROCSAT-1, *J. Geophys. Res.*, *114*, A05308, doi:10.1029/2009JA014060.

Ren, Z., W. Wan, and L. Liu (2009b), GCITEM-IGGCAS: A new global coupled ionosphere-thermosphere-electrodynamics model, *J. Atmos. Sol. Terr. Phys.*, *71*(17–18), 2064–2076, doi:10.1016/j.jastp.2009.09.015.

Ren, Z., W. Wan, J. Xiong, and L. Liu (2010), Simulated wave number 4 structure in equatorial *F* region vertical plasma drifts, *J. Geophys. Res.*, *115*, A05301, doi:10.1029/2009JA014746.

Richards, P. G., M. R. Torr, and D. G. Torr (1982), The seasonal effect of nitric oxide cooling on the thermospheric U.V. heat budget, Planet. *Space Sci.*, *30*(5), 515–518, doi:10.1016/0032-0633(82)90062-9.

Richmond, A. D. (1995), The ionospheric wind dynamo: Effects of its coupling with different atmospheric regions, in *The Upper Mesosphere and Lower Thermosphere: A Review of Experiment and Theory*, *Geophys. Monogr. Ser.*, vol. 87, edited by R. M. Johnson and T. L. Killeen, pp. 49–65, AGU, Washington, D. C.

Russell, J. M., III, M. G. Mlynczak, L. L. Gordley, J. Tansock, and R. Esplin (1999), An overview of the SABER experiment and preliminary calibration results, *Proc. SPIE Int. Soc. Opt. Eng.*, *3756*, 277–288.

Sagawa, E., T. J. Immel, H. U. Frey, and S. B. Mende (2005), Longitudinal structure of the equatorial anomaly in the nighttime ionosphere observed by IMAGE/FUV, *J. Geophys. Res.*, *110*, A11302, doi:10.1029/2004JA010848.

Scherliess, L., D. C. Thompson, and R. W. Schunk (2008), Longitudinal variability of low-latitude total electron content: Tidal influences, *J. Geophys. Res.*, *113*, A01311, doi:10.1029/2007JA012480.

Siskind, D. E. (2000), On the coupling between middle and upper atmospheric odd nitrogen, in *Atmospheric Science Across the Stratopause*, *Geophys. Monogr. Ser.*, vol. 123, edited by D. E. Siskind, S. D. Eckermann, and M. E. Summers, pp. 101–116, AGU, Washington, D. C.

Titheridge, J. E. (1997), Model results for the ionospheric *E* region: Solar and seasonal changes, *Ann. Geophys.*, *15*, 63–78, doi:10.1007/s00585-997-0063-9.

Wan, W., L. Liu, X. Pi, M.-L. Zhang, B. Ning, J. Xiong, and F. Ding (2008), Wavenumber-4 patterns of the total electron content over the

low latitude ionosphere, *Geophys. Res. Lett.*, *35*, L12104, doi:10.1029/2008GL033755.

Zhang, X., J. M. Forbes, M. E. Hagan, J. M. Russell III, S. E. Palo, C. J. Mertens, and M. G. Mlynczak (2006), Monthly tidal temperatures 20–120 km from TIMED/SABER, *J. Geophys. Res.*, *111*, A10S08, doi:10.1029/2005JA011504.

Zhang, Y., S. England, and L. J. Paxton (2010), Thermospheric composition variations due to nonmigrating tides and their effect on ionosphere, *Geophys. Res. Lett.*, *37*, L17103, doi:10.1029/2010GL044313.

L. Liu, Z. Ren, W. Wan, and J. Xiong, Beijing National Observatory of Space Environment, Institute of Geology and Geophysics, Chinese Academy of Sciences, Beitucheng Xilu 19, Beijing 100029, China. (wanw@mail.iggcas.ac.cn)